RESEARCH ARTICLE | JULY 14 2026

A microscopic theory of small-droplet adhesion on solid surfaces

Ruize Yin ; Fei Wang ; Britta Nestler

J. Chem. Phys. 165, 024707 (2026)
https://doi.org/10.1063/5.0337869

The Journal of Chemical Physics ARTICLE pubs.aip.org/aip/jcp

A microscopic theory of small-droplet adhesion on solid surfaces

Cite as: J. Chem. Phys. 165, 024707 (2026); doi: 10.1063/5.0337869
Submitted: 9 April 2026 • Accepted: 17 June 2026 •
Published Online: 14 July 2026 • Publisher Error Corrected: 15 July 2026

Ruize Yin,[1,2] Fei Wang,[1,2,a)] and Britta Nestler[1,2,3]

AFFILIATIONS

[1] Institute for Applied Materials—Microstructure Modelling and Simulation (IAM-MMS), Karlsruhe Institute of Technology (KIT), Strasse am Forum 7, 76131 Karlsruhe, Germany
[2] Institute of Nanotechnology (INT), Karlsruhe Institute of Technology (KIT), Hermann-von-Helmholtz-Platz 1, 76344 Eggenstein-Leopoldshafen, Germany
[3] Institute of Digital Materials Science, Karlsruhe University of Applied Sciences, Moltkestrasse 30, 76133 Karlsruhe, Germany

[a)] **Author to whom correspondence should be addressed:** fei.wang@kit.edu

ABSTRACT

Droplets resting on solid surfaces resist lateral forces before sliding; however, the microscopic origins of the sliding criterion and solid–liquid adhesion remain elusive. Here, we develop a microscopic mean-field theory that incorporates the dependence of solid–liquid interfacial energy on the droplet's body energy and maps the full energy landscape under coupled normal and lateral loads. Within this framework, we propose a sliding criterion within the small-droplet limit, in which the solid–liquid and solid–gas interfacial energies become equal, as a result of the formation of a novel microscopic lubrication-like interfacial state. This criterion explains the observed enhancement of adhesion under increasingly negative normal loads, thereby violating Amontons' first law. Furthermore, we reveal the microscopic origin of pinning force associated with contact angle hysteresis. Our approach eliminates inconsistencies associated with body–force balance in small droplets and achieves quantitative agreement with counterintuitive experimental observations across diverse conditions.

I. INTRODUCTION

Droplets on solid substrates resist lateral forces up to a finite threshold before sliding occurs.[1–3] This behavior is ubiquitous, manifesting in everyday phenomena, such as water droplets shaken off a plate or raindrops adhering to window glass. Droplet adhesion on solid surfaces is also crucial in numerous industrial processes, including printing, coating, and spray deposition.[4,5] Despite its ubiquity and practical importance, the microscopic origin of the sliding criterion and the adhesion force remains poorly understood.[3,6]

Existing theories identify the critical sliding condition by balancing the body force, such as gravity, with an interfacial tension force associated with contact angle hysteresis (CAH).[7–9] This class of approaches includes the widely adopted framework proposed by Kawasaki[10] and Furmidge,[11] known as the Kawasaki–Furmidge (K–F) model. For instance, for a droplet of mass m on a flat plate, the critical roll-off angle θ_{tilt} is described by

$$mg \sin\theta_{tilt} = kW\sigma(\cos\theta_- - \cos\theta_+), \quad (1)$$

where g is the gravitational acceleration, σ is the liquid–vapor surface tension, W is the characteristic width of the droplet footprint (typically measured perpendicular to the direction of motion), and θ_+ and θ_- are the advancing and receding contact angles at the front and rear of the droplet, respectively. The dimensionless parameter k is a geometric factor that accounts for the droplet shape and contact-line geometry (often taken to be of order unity and determined empirically).

However, existing theories based on body–force balance and contact-angle hysteresis (CAH) exhibit three major limitations when applied to predicting static friction:

(I) For small droplets, such as water drops with volumes below ~ 1 μl, the Bond number is much less than unity ($Bo = \triangle\rho R_0^2 g/\sigma \ll 1$, where $\triangle\rho$ is the density contrast, R_0 is a virtual radius with $V = 4/3\pi R_0^3$), and the body energy is negligible compared to the surface energy (Appendix A). Consequently, employing body forces in a force-balance sliding criterion,[12,13] as in the K–F theory,[1] becomes inappropriate.

(II) Despite its broad use, the K–F model struggles to rationalize a number of counterintuitive observations[14] that appear to violate the droplet analog of Amontons' first law of friction.[15] McHale and co-workers showed that an Amontons-like friction law for droplets can, in fact, be obtained from the classical K–F (Furmidge-type) relation via a first-order (linear) expansion, thereby supporting the view that a solid-friction-style description remains meaningful for droplet motion in many cases.[15] However, this connection does not resolve experimental reports in which droplet resistance deviates markedly from Amontons-like scaling, indicating that additional mechanisms beyond the classical K–F picture are required.

(III) When a droplet approaches sliding, it is common to invoke Young's relation at the front and rear contact line to rationalize CAH and the associated adhesion force.[16–19] Strictly, Young's law defines the equilibrium contact angle on an ideal rigid, smooth, chemically homogeneous, and isotropic substrate, provided that the contact line is not pinned and the interface is in thermodynamic equilibrium; under these conditions, the energy-minimizing droplet is axisymmetric [Fig. 1(a)], and the contact angle is uniform, even when body-energy contributions are included.[20] The derivations are given below. Under lateral loading, droplets become asymmetric [Fig. 1(b)] and exhibit apparent advancing and receding angles influenced by pinning[6] and dissipation.[21] Accordingly, these measured angles should be interpreted as non-equilibrium angles rather than Young's angle, and applying Young's law to both sides should be understood as an approximation.[22,23]

Butt and co-workers[21] framed contact-angle hysteresis in dynamic wetting through an "adaptive wetting" mechanism, in which the effective interfacial energy density at the three-phase contact line relaxes exponentially toward equilibrium. This picture attributes the velocity dependence of the advancing and receding angles to microscopic adaptation occurring within a nanometric near-surface region of the solid adjacent to the solid–liquid interface (with a characteristic length scale on the order of 1–100 nm, depending on the underlying process and material[21,24–26]), and it provides a route to connect steady-sliding dissipation with the observed hysteresis, particularly at low speeds. At the same time, the approach still has limitations that leave room for further development. To obtain tractable expressions, their analysis of moving droplets largely relies on an idealized two-dimensional setting, which does not fully capture the geometrical and energetic complexity of real three-dimensional droplets under external forcing. More importantly, the work focuses on droplets that are already in steady motion and does not explicitly address the onset of motion (depinning/start-up), so it does not directly provide predictions for key thresholds such as static adhesion force, critical tilt angle, or incipient sliding conditions. The authors also note that fitting dynamic contact-angle data alone does not uniquely validate the mechanism, and a more unified treatment of the adaptive dynamics with other dissipation mechanisms remains an open direction.

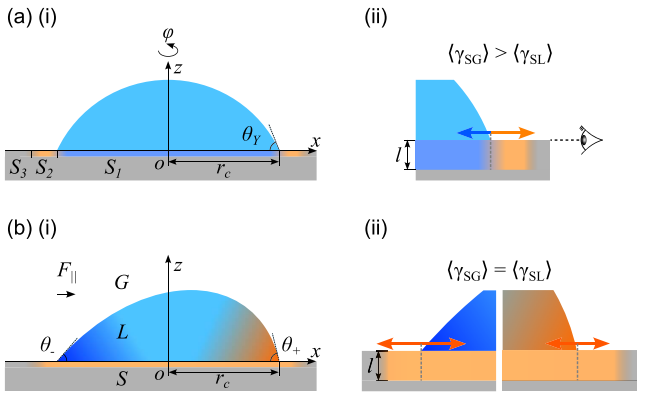

FIG. 1. (a) (i) Schematic cross section of a hydrophilic droplet (L) on a solid substrate (S) in a surrounding gas phase (G), with base radius r_c, Young's contact angle θ_Y, and a colored adsorption layer. S_1 is the wetted area, S_2 denotes the newly introduced droplet-proximity-penetration area outside the apparent contact line, and S_3 represents the far-field unaffected substrate. (ii) Enlarged view of the adsorption layer of thickness l. (b) (i) Droplet under a lateral load $F_\parallel$ at the critical sliding state, with advancing and receding angles θ_+ and θ_-; shaded regions indicate load-induced pressure non-uniformity. (ii) Enlarged view of the region where the averaged solid–liquid and solid–gas interfacial tensions coincide, corresponding to the formation of a microscopic lubrication-like interfacial state.

The slippery liquid-infused porous surfaces (SLIPS)[27] strategy reduces droplet friction by replacing direct contact-line interactions with a heterogeneous solid with interaction occurring at a stabilized liquid interface. In SLIPS, an immiscible lubricant is immobilized within a microporous or textured substrate, creating a physically smooth, chemically uniform "lubricating film" at the surface. By effectively screening the underlying solid heterogeneities, this liquid layer suppresses contact-line pinning, thereby lowering the pinning energy barriers and the resulting contact-angle hysteresis. Consistent with this mechanism, experiments report ultra-low hysteresis for liquids spanning a broad range of surface tensions, indicative of markedly reduced droplet adhesion and a lower threshold for motion. A key limitation, however, is that the low-resistance state depends on an externally supplied, pre-infused lubricant and on its stability against displacement, so SLIPS represents an engineered limiting case rather than a general predictive framework for static friction on conventional lubricant-free solids.

The onset of drop sliding is often defined through local contact-line motion, such as the first detectable displacement of the advancing or receding edge.[14] However, such operational criteria are not unique. For example, de la Madrid *et al.*[2] defined the onset of motion by requiring the receding edge to reach a velocity of ~0.09 mm s^{-1}. Because the local contact angles and pinning states at the advancing and receding sides generally differ, the choice of a local criterion can lead to different apparent sliding thresholds. This ambiguity makes a purely local criterion less suitable as a unique general criterion for macroscopic static friction. This motivates an energy-based description in which the critical state is identified from the global free energy of the droplet–substrate system, while local variations in the interfacial energy are incorporated through mean field theory in the form of spatial averaging.

In this article, we propose a microscopic, load-dependent framework for predicting solid–liquid adhesion by explicitly tracking how externally applied normal and lateral loads modify the solid–liquid interfacial energetics. Departing from conventional macroscopic descriptions that forces against a CAH-based friction

law, we build our approach on the adsorption layer concept,[28,29] in which interfacial energy density changes arise from load-driven variations in adsorption-layer composition governed by the free-energy minimization principle. In contrast to macroscopic SLIPS, when the composition distribution within the microscopic adsorption layer becomes symmetric across the three-phase contact line, the layer enters a microscopic lubrication-like interfacial state formed by the droplet liquid itself.

The microscopic lubrication-like interfacial state proposed here should not be understood as a macroscopically observable, geometrically continuous liquid layer with a prescribed finite thickness and hydrodynamic fluidity.[27] It instead denotes an effective interfacial condition within the adsorption layer,[28] realized when the energetic asymmetry between the liquid-covered and gas-covered adsorption-layer regions vanishes. Under this condition, the two sides of the contact-line region become energetically equivalent so that interfacial exchange can occur without an additional free-energy cost. An adsorption layer satisfying this condition is, therefore, referred to here as an energetically symmetric adsorption layer. This interpretation defines the physical meaning of the microscopic lubrication-like state in the present theory.

We associate the onset of motion with the first formation of this state, which marks the transition from a pinned regime to a mobile one. This perspective yields a load-controlled and experimentally testable lubrication–transition criterion for sliding that does not rely on an added lubricant but instead on the energetic accessibility of a microscopic lubrication-like interfacial state configuration under external loading.

The resulting framework maps the droplet free-energy landscape under coupled normal and lateral loads and identifies a transition pathway from equilibrium to incipient sliding. It further motivates a critical-state criterion for small droplets on ideal rigid surfaces: the asymmetry between the appropriately averaged solid–liquid and solid–gas interfacial free-energy densities at the substrate interface vanishes, concomitant with the formation of a microscopic lubrication-like state.[27,30,31] Unlike SLIPS, which achieves low friction via a porous substrate infused with an external lubricant,[27] our approach emphasizes a microscopic, load-induced interfacial reconstruction mechanism. This criterion explains why increasing the normal load may lead to a non-monotonic adhesion response, which differs from the monotonic behavior expected from the droplet analog of Amontons' first law of friction. The classical Kawasaki–Furmidge relation is recovered as a limiting case, and the same criterion provides a microscopic interpretation of CAH that is in quantitative agreement with diverse experimental datasets.[14,32,33]

II. METHOD

We consider a stationary droplet of fixed volume V on an ideally flat and rigid substrate.

The total interfacial energy of the system is written as

$$E = \sigma A - \int_{S_1} \triangle\gamma \mathrm{d}S_1 + \int_{S_2^*} \gamma_{SG} \mathrm{d}S_2^* + \int_{S_3} \gamma_{SG}^* \mathrm{d}S_3. \tag{2}$$

Here, the first term is the liquid–gas interface contribution, with interfacial tension σ and cap area A. The second term is the wetting contribution over the wetted area S_1, given by the surface integral of the interfacial-tension difference, $\triangle\gamma \equiv \gamma_{SG} - \gamma_{SL}$ (solid–gas interfacial tension minus solid–liquid interfacial tension). In contrast to the conventional assumption of a constant $\triangle\gamma$, we consider its modification under external loads, such as gravity. This adjustment stems from defining a spreading area $S_2^* = S_1 + S_2$, which combines the wetted area S_1 with the droplet proximity penetration area S_2 located outside the apparent triple line [Fig. 1(a), yellow].[29] The third and fourth terms represent the interfacial energies of the droplet–proximity penetration region, S_2^*, and the far-field unaffected area, S_3 (γ_{SG}^* is the intrinsic solid–gas interfacial tension), respectively; both serve as constant references,[28 and 34] and they are, therefore, excluded from the following derivations.

For small droplets resting on solid substrates with a Bond number much less than unity ($Bo \ll 1$), gravitational (body) energy is negligible compared with interfacial energy.[35,36] As a result, gravity does not appreciably distort the droplet from a spherical-cap shape. Under this spherical-cap (axisymmetric) assumption, the total interfacial free energy can be written as

$$\begin{aligned} E &= \int_0^{2\pi} \int_0^{r_c} r \left[\sigma \sqrt{1 + \left(\frac{\mathrm{d}h}{\mathrm{d}r}\right)^2} - \triangle\gamma \right] \mathrm{d}r\mathrm{d}\varphi \\ &= \sigma 2\pi (r_c/\sin\theta)^2 (1 - \cos\theta) - \triangle\gamma \pi r_c^2, \end{aligned} \tag{3}$$

where θ is the (macroscopic) contact angle and r_c is the contact radius.

Using the spherical-cap volume relation

$$V = \frac{\pi}{3}\left(\frac{r_c}{\sin\theta}\right)^3 (2 + \cos\theta)(1 - \cos\theta)^2,$$

one obtains the θ–r_c relation

$$r_c = \left[\frac{3V}{\pi(2 + \cos\theta)(1 - \cos\theta)^2} \right]^{1/3} \sin\theta. \tag{4}$$

Substituting this expression into Eq. (3) yields the total energy as a function of θ alone,

$$E = [2\sigma - \triangle\gamma(1 + \cos\theta)] \left[\frac{9\pi V^2}{(2 + \cos\theta)^2 (1 - \cos\theta)} \right]^{\frac{1}{3}}. \tag{5}$$

Minimizing the interfacial free energy with respect to the contact angle, $\mathrm{d}E/\mathrm{d}\theta = 0$, leads to the classical Young relation

$$\sigma \cos\theta_Y = \gamma_{SG} - \gamma_{SL} \quad (\text{i.e., } \cos\theta_Y = \triangle\gamma/\sigma). \tag{6}$$

This energy-minimization derivation, therefore, defines the equilibrium contact angle, θ_Y, which is uniform along the entire three-phase contact line for an axisymmetric droplet at thermodynamic equilibrium [Fig. 1(a)]. Because these assumptions are essential to the derivation, the applicability of Young's law should be intrinsically limited to describing droplets in thermodynamic equilibrium on ideal, smooth, chemically homogeneous surfaces.

When a lateral load $F_\parallel$ is applied, the droplet withstands the load and remains pinned in place. As $F_\parallel$ increases, the droplet approaches a critical sliding condition. Traditionally, this critical condition is identified by a force balance, i.e., when the applied lateral load equals the droplet's maximum adhesive (retention) force.

At this critical state, the droplet becomes asymmetric, giving rise to two distinct apparent contact angles: θ_+ and θ_- at the advancing and receding edges, respectively [Fig. 1(b)]. Up to the onset of macroscopic motion, the droplet is treated as stationary; therefore, its macroscopic kinetic energy is neglected.

Following the discussion above, interfacial contributions dominate the energetics of small droplets. For a laterally loaded (and thus non-axisymmetric) droplet, Young's-law conditions are no longer satisfied, and the local interfacial energy difference $(\gamma_{SL} - \gamma_{SG})$ is not uniform over the contact region. Therefore, applying Eq. (2) together with the mean value theorem for integrals, we express the system energy in an averaged form as

$$E \equiv E_{\text{cap}} + E_{\text{base}} = \sigma A + \langle \gamma_{SL} - \gamma_{SG} \rangle S_1 = \sigma A - \langle \triangle \gamma \rangle S_1, \tag{7}$$

where A is the liquid–vapor surface area, S_1 is the base area, and $\langle \cdot \rangle$ denotes the spatial average over S_1.

In the small-droplet limit, the change in A from the Young-equilibrium $(\theta = \theta_Y)$ state to the critical sliding state is minor (Appendix A). Hence, $E_{\text{cap}} = \sigma A$ can be treated as approximately constant, and the energy variation is dominated by the base contribution, $E_{\text{base}} = -\langle \triangle \gamma \rangle S_1$.

A. Surface composition effect

The introduction of an adsorption layer is motivated by the long-standing diffuse-interface view of interfacial thermodynamics. In the Gibbs construction,[37] the boundary between two phases is idealized as a mathematical dividing surface. The interfacial free energy is then formulated in terms of surface excess quantities associated with this dividing surface. These quantities represent the excess amount of a substance per unit interfacial area relative to the extrapolated bulk phases and, therefore, describe an interfacial composition that generally differs from the corresponding bulk concentrations.[37]

By contrast, van der Waals formulated capillarity under the hypothesis of a continuous variation of density, in which the interface is regarded as a finite transition region rather than a zero-thickness discontinuity.[38,39] In such a region, the local energy cannot be determined solely by the density at a point, because molecules interact with their surrounding molecular neighborhood over a finite range. Therefore, when the density or composition varies rapidly near an interface, the local free energy must also depend on the spatial distribution of the neighboring density or composition field. This nonlocal molecular contribution naturally gives rise to the diffuse-interface description, in which the equilibrium interfacial profile is determined by the minimization of a free-energy functional rather than prescribed as an abrupt jump. From this perspective, the diffuse-interface formulation may be viewed as a more structurally resolved representation of the same interfacial thermodynamics described by the Gibbs construction. Thus, although the two descriptions differ in how the interface is represented geometrically, both emphasize that the composition of the interfacial region can strongly affect the interfacial free energy, or equivalently the surface tension.

This idea was later formalized in Cahn's diffuse-interface theory,[40,41] where the free energy of a nonuniform system is written, to leading order, as a local homogeneous contribution plus a gradient-energy contribution, namely,

$$E_{free} = \int_V \left[f_0(c) + \frac{\kappa}{2} |\nabla c|^2 \right] \mathrm{d}V, \tag{8}$$

where c is the local composition or concentration, $f_0(c)$ is the homogeneous free-energy density, and κ is the gradient-energy coefficient. Within this framework, the interfacial tension is determined by the excess free energy stored in the finite inhomogeneous layer and is, therefore, naturally sensitive to the local composition and structure of this layer.[42–44] Cahn's theory further demonstrated that a surface layer of the wetting phase may persist even when that phase is no longer stable as a bulk phase, indicating that the thermodynamic state of a surface-adjacent region can differ from that of either adjoining bulk phase.[40,45]

Molecular-dynamics simulations[46–52] provide direct microscopic support for this finite interfacial-layer picture. For example, large-scale simulations of Lennard-Jones liquid–vapor interfaces showed a continuous interfacial density profile with a finite apparent width, rather than a discontinuous density jump between the two bulk phases.[46–49] At solid–fluid boundaries, molecular-dynamics simulations of Lennard-Jones fluids adsorbed on structured solid substrates obtained spatially resolved density profiles near the wall and identified a structured adsorption region adjacent to the substrate, together with wetting and drying transitions determined from surface tensions and contact angles.[50–52] These results suggest that the microscopic boundary near a solid substrate is better regarded as a finite transition region with spatially varying density or composition than as an ideal sharp discontinuity.

Experimental wetting studies[26,53,54] also support the existence of finite interfacial or adsorbed layers whose thickness depends on thermodynamic conditions. In the wetting-transition experiments reviewed by Bonn and co-workers,[26] the adsorbed film adjacent to a droplet may undergo either a discontinuous thin-to-thick jump in a first-order wetting transition or a continuous growth of thickness in critical wetting, reflecting the thermodynamic coupling between surface free energy, long-range intermolecular interactions, and temperature. In methanol/n-alkane systems, where n-alkane denotes a straight-chain alkane, measurements of the contact angle and wetting-layer thickness further revealed a crossover from first-order wetting to critical wetting upon approaching the bulk liquid–liquid critical point.[53] Beyond Bonn's work, complete-to-partial wetting transitions near critical points and complete-wetting layers at polymer–air interfaces have also been observed experimentally.[54] These theoretical, numerical, and experimental observations justify treating the solid-adjacent interfacial region not as a purely geometrical boundary but as a finite adsorption layer with its own thermodynamic state.

In the present work, this interfacial region is described, within a mean-field framework, as an adsorption layer separating the two bulk phases.[28,29] The state of the adsorption layer is characterized by the volume fraction ϕ of liquid phase in the liquid–gas mixture within the adsorption layer [see Figs. 1(a-ii) and 1(b-ii)]. This representation suggests that both the composition of the adsorption layer and its internal energetic state, as modified by the external loading environment, can influence the local excess free energy and

hence the corresponding interfacial tension.[37,55] Accordingly, the free energy of the adsorption layer is formulated as

$$\gamma = l[\varepsilon(\phi) + \chi(\phi) + p(\phi)], \tag{9}$$

where l is the effective thickness of the adsorption layer,[21,56,57] while ε, χ, and p denote the internal energy, van der Waals interaction energy, and pressure energy (Appendix B), respectively.

Following Wang's work,[28,29] this dependence is written as

$$\begin{aligned} \varepsilon(\phi) &= f_s[\varepsilon_L\phi + \varepsilon_G(1-\phi)], \\ \chi(\phi) &= \chi_{LG}\phi(1-\phi) + f_s[\chi_{SL}\phi + \chi_{SG}(1-\phi)], \\ p(\phi) &= f_s[p_L\phi + p_G(1-\phi)]. \end{aligned} \tag{10}$$

Here, ε_L and ε_G denote the volumetric internal energies of the liquid and gas, respectively. χ_{LG}, χ_{SL}, and χ_{SG} are the van der Waals interaction parameters for the liquid–gas, solid–liquid, and solid–gas pairs, respectively.[37] The liquid-phase pressure is

$$p_L = p_G + 2\frac{\sigma}{R} + \frac{\rho V a_\perp}{\pi r_c^2}.$$

Here, p_G is the gas-phase pressure, R is the curvature radius of the droplet's liquid–gas interface, and ρ is the liquid density. f_S serves as a correction factor to Dalton's law of partial pressures (Appendix C).

In the present framework, the substrate regions beneath the liquid and beneath the gas are both treated as the same adsorption-layer phase composed of the same solid, liquid, and gas constituents. Since the underlying forms of internal energy and intermolecular interactions are, therefore, of the same physical origin, the corresponding interfacial free energies are described by the same constitutive function with the same set of material parameters. Rearranging the terms, we obtain

$$\frac{\gamma}{l\chi_{LG}} = -\phi^2 + \left(\alpha + \frac{f_S\rho V}{\pi r_c^2\chi_{LG}}a_\perp\right)\phi + \frac{\beta}{\chi_{LG}}, \tag{11}$$

where $\alpha = 1 - f_S(\triangle\varepsilon + \triangle\chi - 2\sigma/R)/\chi_{LG}$ and $\beta = f_S(\varepsilon_G + \chi_{SG} + p_G)$. Here, we define $\triangle\varepsilon = \varepsilon_G - \varepsilon_L$ and $\triangle\chi = \chi_{SG} - \chi_{SL}$. Since α is constructed from the parameters characterizing the droplet in the absence of external loading, it represents the intrinsic surface-energy contribution. Detailed discussions of the role of each term are given in the works of Wang *et al.*[28,29,58]

To evaluate the normal load-induced pressure, we introduce a signed normal acceleration $a_\perp$ (positive for sessile and negative for pendant). Variations in $a_\perp$ adjust the internal liquid pressure and, crucially, reshape the adsorption-layer composition.[59,60] These composition changes, in turn, modulate the interfacial energy densities at the solid–liquid interface of wetted area S_1 and at the solid–gas interface of droplet-affected area S_2. Accordingly, we define the solid–liquid and solid–gas interfacial energies as $\gamma_{SL} = \gamma(\phi_L)$ and $\gamma_{SG} = \gamma(\phi_G)$. The corresponding average values are

$$\langle\gamma_{SL}\rangle = \gamma(\langle\phi_L\rangle),\ \langle\gamma_{SG}\rangle = \gamma(\langle\phi_G\rangle). \tag{12}$$

Here, ϕ_L and ϕ_G represent the equilibrium volume concentrations of the liquid in the regions S_1 and S_2, respectively; $\langle\phi_L\rangle = {S_1}^{-1}\int_{S_1}\phi_L dS_1$ and $\langle\phi_G\rangle = {S_2}^{-1}\int_{S_2}\phi_G dS_2$ denote the average values.

Here, ϕ_L and ϕ_G represent the liquid volume fractions in the adsorption layer in two spatially distinct regions: the droplet-covered region and the surrounding gas-covered region, respectively. The two variables, ϕ_L and ϕ_G, are treated as independent degrees of freedom. This treatment is analogous to the classical composition phase diagram of an immiscible binary fluid, in which a unified free-energy formulation is used to describe the thermodynamic state of the system, while the compositions of the coexisting phases are treated as independent variables. Their equilibrium values are then determined through minimization of the total free energy.

Notably, Butt *et al.*[21] developed an adaptive-wetting framework for polymeric substrates, in which near-surface interfacial properties relax exponentially toward equilibrium on a finite adaptation timescale,

$$\gamma_i(t) = \gamma_i^\infty + \gamma_i^* e^{-t/\tau_i}.$$

Here, i can take the values SG, SL, and LG, representing the solid–gas, solid–liquid, and liquid–gas interfacial tensions, respectively. In this description, $\gamma_i(t)$ denotes the time-dependent interfacial tension, γ_i^∞ is the corresponding long-time equilibrium value, γ_i^* is the difference between the initial value at $t = 0$ and the equilibrium value at $t \to \infty$, and τ_i is the characteristic timescale of the adaptation process.

Building on these relaxation dynamics, they described the front–rear asymmetry of interfacial tensions during steady sliding and attributed the velocity dependence of the advancing and receding contact angles to the fact that the two sides experience different adaptation times as the contact line moves. The characteristic timescale τ, therefore, governs the adaptation rate and, in turn, influences the resulting contact-angle hysteresis. A direct implication of this formulation is that, for a static droplet on an ideal homogeneous and flat substrate, both sides eventually relax to the same long-time equilibrium interfacial state, γ_i^∞, so that the front–rear asymmetry vanishes. Within this mechanism alone, persistent static hysteresis is, therefore, not expected. The underlying adaptation length scale is often associated with a nanometric near-surface region, whose effective depth may grow in a diffusion-like manner, often with a Washburn-type[57] penetration.

In contrast, the present work focuses on how composition-dependent equilibrium interfacial energetics, modified by external loading, determine the limiting static states of the droplet and the emergence of static hysteresis. We further identify the critical sliding condition as the point at which an energetically symmetric adsorption-layer configuration first becomes both thermodynamically accessible and stable. In this way, the present theory bridges the pinned state and the onset of motion.

For equilibrium interfacial energetics, Cahn,[45] De Gennes,[9] and many later studies[26,42] developed phase-field descriptions of wetting. In Cahn's theory, the equilibrium surface free energy is obtained by minimizing a free-energy functional for a semi-infinite fluid near an ideal planar wall. The functional includes a surface term set by the composition at the wall, a bulk term describing the deviation of the local composition from the bulk value, and a square-gradient term that suppresses sharp spatial changes in composition.

Under the far-field condition that the composition recovers its bulk value, variational minimization of Eq. (8) yields both the

one-dimensional composition profile normal to the surface and the natural equilibrium boundary condition at the wall,

$$\frac{d\Phi}{dc_s} - 2\kappa\left(\frac{dc}{dy}\right)_s = 0,$$

where $c = c(y)$ is the composition field of the fluid, y is the coordinate normal to the solid surface, $c_s \equiv c(0)$ is the limiting composition at the wall, $\Phi(c_s)$ is the surface free-energy contribution per unit area of the solid in contact with a fluid of wall composition c_s, and $(dc/dy)_s \equiv \lim_{y\to 0} dc/dy$ denotes the concentration gradient evaluated at the wall.

In this sense, Cahn's theory may be viewed as describing the equilibrium limit of the interfacial composition and energetics, i.e., the long-time state corresponding to γ_i^{∞} in the adaptive-wetting picture of Butt *et al.* The resulting surface free energy is determined by a smooth equilibrium composition profile that minimizes the free-energy functional while simultaneously satisfying the boundary conditions on both the interfacial energetics and the material distribution at an ideal planar substrate.

However, our work does not resolve a local planar adsorption profile. Instead, we treat the surface energy as composition dependent and determine the material distribution by minimizing the total interfacial energy of the entire droplet under volume constraint and external loading. This global framework is more appropriate for finite droplets, whose state is governed by the coupled effects of composition, geometry, and load. It thus provides a direct and thermodynamically consistent description of the equilibrium distribution, the limiting static states, and the onset of sliding.

B. Energy landscape and extrema values

The total interfacial energy of the droplet is obtained by substituting the surface-tension function in Eq. (11) into the energy expression in Eq. (7). As noted above, the energy contribution from the droplet cap, E_{cap}, is treated as approximately constant. The following analysis, therefore, focuses on the energy contribution from the droplet base,

$$\begin{aligned} E_{base} &= (\gamma\langle\phi_L\rangle - \gamma\langle\phi_G\rangle)\pi r_c^2 \\ &= l\chi_{LG}\left[\langle\phi_G\rangle^2 - \langle\phi_L\rangle^2 + 2\eta(\langle\phi_L\rangle - \langle\phi_G\rangle)\right]\pi r_c^2, \end{aligned} \tag{13}$$

with

$$2\eta = \alpha + f_S\rho V a_\perp/(\pi r_c^2\chi_{LG}).$$

Here, the parameter η contains two contributions: the intrinsic parameter α, which characterizes the surface energetics discussed above, and an additional term arising from the external load. Accordingly, η is taken to represent an effective total surface-energy parameter. The effects of the parameters α and η are discussed in detail below. In applying the model to experiments, the macroscopic quantities V, ρ, σ, θ_Y, and $a_\perp$ are taken from the measured system. The normal acceleration $a_\perp$ is prescribed by the actual loading condition, for example, $a_\perp = +g$ for a sessile droplet and $a_\perp = -g$ for a pendant droplet. The microscopic quantities entering α, such as ε, χ, l, f_S, and χ_{LG}, are not

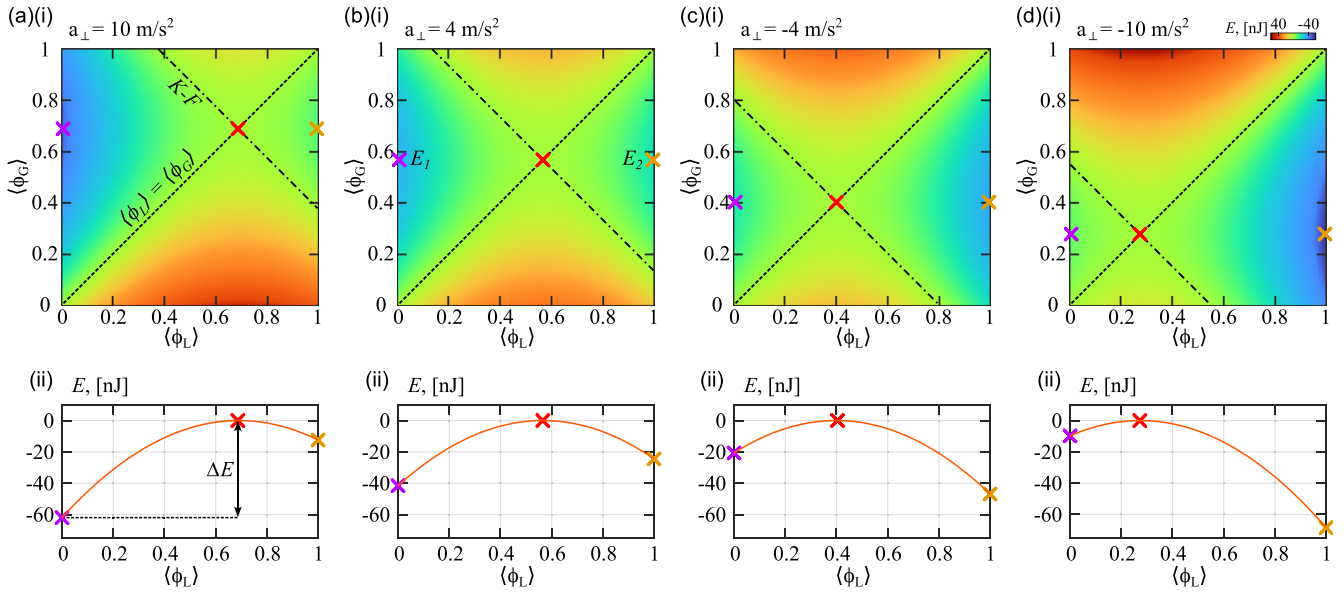

FIG. 2. Energy landscapes of $E_{base}(\langle\phi_L\rangle, \langle\phi_G\rangle)$ for different normal loads $a_\perp$. Each surface is saddle-shaped, with the central profile varying with $a_\perp$: (a) sessile, $a_\perp$ = 10 ms^{-2}; (b) semi-sessile, $a_\perp$ = 4 ms^{-2}; (c) semi-pendant, $a_\perp$ = −4 ms^{-2}; and (d) pendant, $a_\perp$ = −10 ms^{-2}. E_S (red cross) marks the saddle point; E_1 (purple) and E_2 (orange) are the local minima at $\langle\phi_L\rangle$ = 0 and $\langle\phi_L\rangle$ = 1, respectively. $\langle\cdot\rangle$ denotes the spatial average. The dashed line denotes $\langle\phi_L\rangle = \langle\phi_G\rangle$ and the dashed-dotted line corresponds to the K–F model. The second-row panels illustrate, for each prescribed normal load, the quasi-static evolution of the system from a local energy extremum toward the saddle point, together with the corresponding variation of the total energy along this pathway. The energy difference between the lowest-energy local extremum and the saddle point is defined as $\triangle E$.

separately available from the reported experiments; therefore, their combined contribution is represented by an effective intrinsic parameter α, calibrated from a reference equilibrium state, such as the measured Young contact angle. Once this reference state is fixed, η varies with $a_\perp$ according to Eq. (13) and is not fitted independently for each loading condition.

For each normal acceleration $a_\perp$, an energy landscape of the droplet's base is obtained from the energy expression Eq. (13) by systematically varying the two microscopic parameters, $\langle\phi_L\rangle$ and $\langle\phi_G\rangle$, within the physical interval $\langle\phi_L\rangle, \langle\phi_G\rangle \in [0,1]$, as shown in Fig. 2. In each case, the energy map $E_{\text{base}}(\langle\phi_L\rangle, \langle\phi_G\rangle)$ forms a saddle-shaped landscape. The energy extreme states are determined by solving the equation system: $\partial E_{\text{base}}/\partial\langle\phi_L\rangle = 0$ and $\partial E_{\text{base}}/\partial\langle\phi_G\rangle = 0$. Two local energy minimum states, $E_1 : \langle\phi_L\rangle = 0, \langle\phi_G\rangle = \eta$ (purple cross); $E_2 : \langle\phi_L\rangle = 1, \langle\phi_G\rangle = \eta$ (orange cross); and a saddle point, $E_S : \langle\phi_L\rangle = \eta, \langle\phi_G\rangle = \eta$ (red cross), are obtained. The saddle point possesses the property of $\langle\triangle\gamma\rangle = 0$. At the sessile state, the global energy minimum occurs at E_1, with $\langle\phi_L\rangle = 0$ [Fig. 2(a)]; whereas at the pendant state, the global energy minimum emerges at E_2 with $\langle\phi_L\rangle = 1$ [Fig. 2(d)].

The energy landscape captures the full evolution of the droplet's energy state from initial deposition to the sliding threshold. By energy minimization, when a droplet is initially placed on a solid substrate, the local energy state at different points within the solid–liquid contact area may be distributed across the energy landscape and relax toward nearby local minima in a gradient-descent-like manner. However, because the droplet forms a continuous and mechanically coupled body, once any region reaches the global minimum, the resulting redistribution drives the entire droplet toward the same global minimum state, at which the droplet adopts the Young contact angle, θ_Y. The transition by which local energy states overcome a higher energy barrier may be viewed, qualitatively, as analogous to a siphon effect, whereby the relaxation of one region into the lower-energy branch facilitates the collective evolution of the entire droplet toward the final global minimum. When a lateral load is applied, the resulting transverse pressure non-uniformity alters the local composition of the adsorption layers, thereby modifying the interfacial tensions over the proximity penetration area S_2^* [Fig. 6 in Appendix A], leading to a spatial variation in $\triangle\gamma$.

Under a quasi-static loading process, the system relaxes to the nearest accessible local minimum at each step, so the energy state follows a single energy-valley branch and the interfacial potential increases monotonically. The system remains stable until the interfacial potential attains its pathwise maximum, as it reaches the saddle point where the along-valley derivative is zero. At the saddle point, the average solid–liquid and solid–gas interfacial tensions on the two sides of the contact line are symmetric ($\langle\triangle\gamma\rangle = 0$), effectively behaving as if the droplet were resting on an energetically symmetric adsorption-layer so that even infinitesimal perturbations can trigger sliding. Beyond this point, sliding ensues, known as dynamic wetting, which is outside the scope of this work.[3]

III. RESULTS AND DISCUSSION

In this section, we discuss the main implications of the present energy-based framework for droplet adhesion and critical sliding. We organize the analysis around three aspects: the dependence of adhesion on the applied normal load, the relation between the present theory and the classical Kawasaki–Furmidge description, and the interpretation of the pinning force and contact-angle hysteresis within the present energy landscape. Together, these results illustrate how the model connects load-dependent interfacial energetics to macroscopic adhesion behavior.

A. Adhesion force prediction

By Amontons' first law, increasing the normal load should increase the static friction, so a sessile droplet would be expected to exhibit a higher sliding threshold. Yet experiments report the opposite trend: a pendant droplet can sustain a larger lateral forcing before sliding than a sessile droplet. This contrast suggests that droplet "friction" is not governed by an Amontons-type load law. In our framework, droplet adhesion is controlled by the energetic barrier separating the metastable minimum from the relevant saddle point. We define this barrier as

$$\triangle E \equiv E_S - \min(E_1, E_2),$$

which must be overcome to initiate sliding. Consequently, the ratio between the lateral adhesion force under a prescribed normal load $a_\perp$ and that under the reference normal load $+g$ can be approximated by the corresponding ratio of energy barriers, as shown in Appendix D,

$$\Lambda = \frac{F_{\parallel a_\perp}}{F_{\parallel +g}} \approx \frac{\triangle E_{a_\perp}}{\triangle E_{+g}}. \tag{14}$$

In our formulation, the local variation of the interfacial energy is not neglected. Rather, it is incorporated into the total base energy as written in Eq. (7). Thus, $\langle\Delta\gamma\rangle$ is not introduced to assume spatial uniformity but to represent the net interfacial-energy contribution controlling the stability of the whole droplet. Local contact-line effects are further retained in the pressure-induced angular variation and the pinning-force distribution, as discussed later. Therefore, the averaged criterion describes the global energetic threshold, while local contact-line processes determine how this threshold is approached.

Within the present framework, two parameters play central roles in determining how droplet adhesion varies with the applied normal load. The parameter α characterizes the intrinsic contribution of the interfacial energetics, whereas η represents an effective total surface-energy parameter that contains both the intrinsic part and the load-induced contribution. As shown in Appendix D, α primarily controls the position of the symmetry axis of the adhesion curve relative to $a_\perp = 0$, reflecting the intrinsic bias introduced by the surface-energy contribution. By contrast, the ratio $\alpha/2\eta_{+g}$, where η_{+g} denotes the value of η at $a_\perp = +g$, measures the relative importance of the intrinsic contribution compared with the load-induced one and, therefore, controls the overall sensitivity of the adhesion to normal loading. A smaller $\alpha/2\eta_{+g}$ means that the external load has a stronger influence on the total surface energy, whereas a larger value indicates that the intrinsic surface energetics dominate and the effect of normal loading becomes weaker.

Figure 3 shows the ratio of lateral adhesion relative to that in the sessile state, Λ, as a function of the normal load $a_\perp$, with $a_\perp \in [-g, +g]$. To illustrate the role of the model parameters, α is varied from 0.8 to 2.0. In Wang's work,[28] $\alpha = 1$ is taken as the reference value for a neutral system. Moreover, since the internal energy of

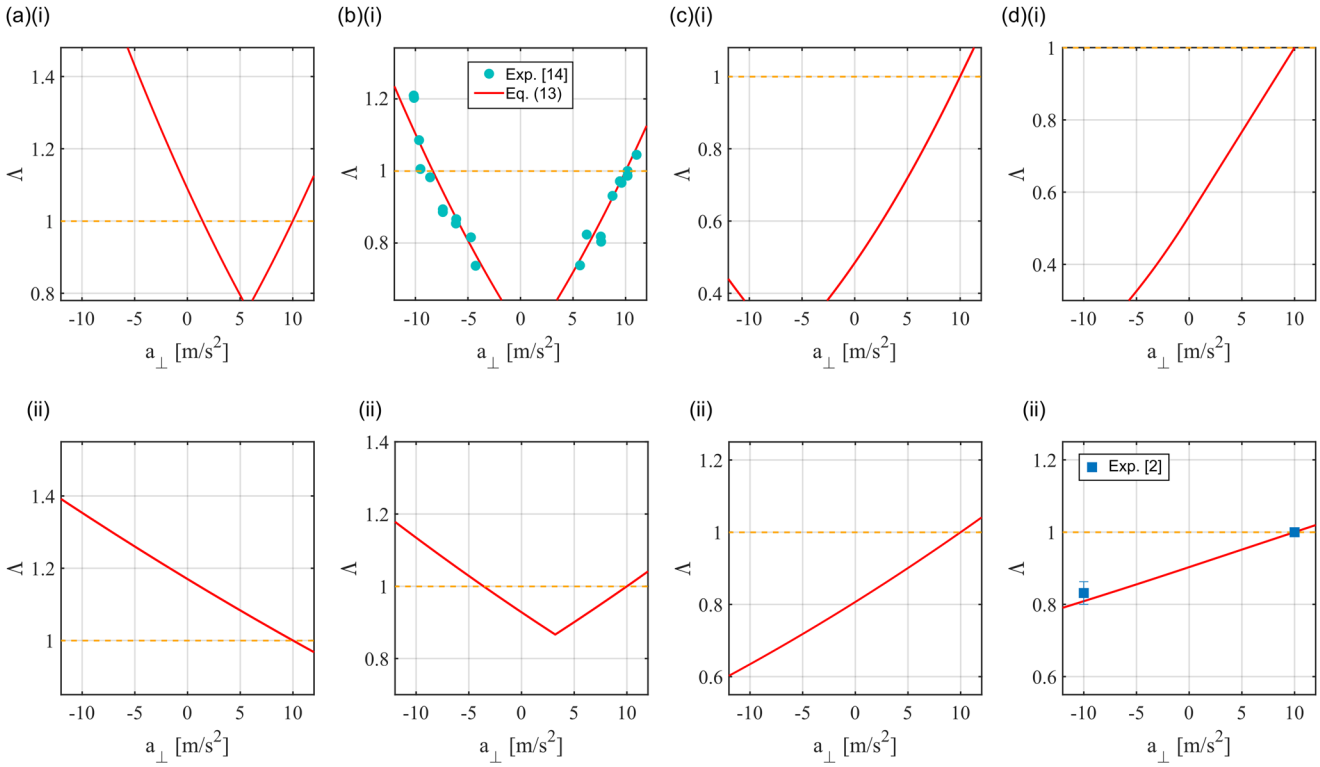

FIG. 3. Ratio of lateral adhesion force as a function of normal load under different parameter settings. The red solid curves show the lateral adhesion-force ratio vs normal load. Here, α varies from 0.8 to 2.0, while the ratio $\alpha/2\eta_{+g}$ is set to 0.7, 0.9, and, for one special case, 0.95. As α deviates from 1, the symmetry axis of the adhesion–load curve shifts away from $a_\perp = 0$, moving toward negative $a_\perp$ for $\alpha > 1$ and toward positive $a_\perp$ for $\alpha < 1$. Larger values of $\alpha/2\eta_{+g}$ indicate a weaker contribution of external loading to the total surface energy and, therefore, lead to gentler slopes. Solid dots represent experimental data from Tadmor's experiment[14] in panel (b) (i) and from Madrid's experiment[2] in panel (d) (ii). The orange dashed line denotes the reference level $F_{\|_{+g}}$. (a) (i) $\alpha = 0.8$, $\alpha/2\eta_{+g} = 0.7$. (ii) $\alpha = 0.8$, $\alpha/2\eta_{+g} = 0.9$. (b) (i) $\alpha = 0.965$, $\alpha/2\eta_{+g} = 0.7$. (ii) $\alpha = 0.965$, $\alpha/2\eta_{+g} = 0.9$. (c) (i) $\alpha = 1.4$, $\alpha/2\eta_{+g} = 0.7$. (ii) $\alpha = 1.4$, $\alpha/2\eta_{+g} = 0.9$. (d) (i) $\alpha = 2$, $\alpha/2\eta_{+g} = 0.7$. (ii) $\alpha = 2$, $\alpha/2\eta_{+g} = 0.95$.

the liquid phase is usually higher than that of the gas phase, $\triangle\varepsilon < 0$, and the Laplace pressure inside the droplet is positive, $2\sigma/R > 0$, the range of α is chosen to extend further on the positive side of unity. The representative values of $\alpha/2\eta_{+g}$ are chosen as 0.7, 0.9, and, for one special case, 0.95, in order to illustrate how different sensitivities to external loading affect the adhesion force in different systems. These parameter settings allow us to examine how the intrinsic interfacial energetics and the load-induced surface-energy contribution each shape the adhesion–normal-load relation.

Several general trends can be identified from Fig. 3. First, as α deviates from 1, the symmetry axis of the adhesion–load curve shifts away from $a_\perp = 0$. In particular, it shifts toward negative $a_\perp$ for $\alpha > 1$ and toward positive $a_\perp$ for $\alpha < 1$. This indicates that α controls the intrinsic bias in the total surface energy and, therefore, determines the load about which the adhesion response is centered. Second, as $\alpha/2\eta_{+g}$ increases, the effect of external loading becomes weaker and the adhesion curves become less steep. Physically, this means that when the intrinsic surface energetics dominate, the normal load perturbs the interfacial state only weakly. By contrast, when $\alpha/2\eta_{+g}$ is smaller, the load-induced contribution becomes more important, and the adhesion becomes more sensitive to $a_\perp$.

For parameter combinations with $\alpha = 0.8$ and $\alpha/2\eta_{+g} = 0.9$, for the parameter set shown in Fig. 3(a-ii), the model predicts that adhesion decreases as the normal load increases from negative to positive values. In other words, a stronger upward pulling force in the pendant direction leads to stronger adhesion. This trend is consistent with the interpretation proposed by McHale *et al.*[15] In their droplet analog of Amontons' law, the normal force N in the relation $F = \mu N$ is associated with the vertical component of the surface tension, i.e., the force acting away from the substrate. Under this interpretation, a larger negative normal force leads to a larger friction term and, hence, stronger droplet adhesion, in agreement with the present result for this parameter setting.

In the experimentally relevant small-droplet regime [Fig. 3(b-i)], the parameters are chosen for a 0.5 μl hexadecane droplet on octadecyltrimethylammonium (OTA)-treated mica, consistent with the experiments reported by Tadmor,[14] for which we take $\alpha = 0.965$ and $\alpha/2\eta_{+g} = 0.7$. The model predicts a non-monotonic dependence on $a_\perp$: smaller $|a_\perp|$ leads to weaker adhesion, while larger $|a_\perp|$ deepens the energy minimum and, therefore, increases the barrier against sliding. As a result, the pendant state $(a_\perp = -g)$ can sustain a lateral adhesion force about 1.1 times that of the sessile state $(a_\perp = +g)$, in

agreement with the experiment. This behavior directly reflects the central idea of the present framework: adhesion is governed by the load-dependent interfacial energy landscape rather than by a purely macroscopic force balance.

Other parameter combinations, such as those in Figs. 3(c-ii), 3(d-i), and 3(d-ii), recover an Amontons-like trend, in which adhesion increases with increasing normal load. In these cases, the normal load effectively stabilizes the pinned state, and the slope of the adhesion curve plays a role analogous to the friction coefficient μ in Amontons' law. Accordingly, the comparison with experimental data[2] can be captured by adopting $\alpha = 2$ and $\alpha/2\eta_{+g} = 0.95$, as in Fig. 3(d-ii). Within the present model, however, this slope is not introduced as an empirical constant. Instead, it emerges naturally from the competition between the intrinsic interfacial energetics and the load-induced contribution, as controlled by α and η.

The variation of these parameters can also be associated with different physical situations. Smaller values of $\alpha/2\eta_{+g}$ correspond to cases in which the effective surface energy is highly sensitive to external loading, so that the applied normal load produces a stronger modification of the interfacial state. Larger values of $\alpha/2\eta_{+g}$, by contrast, describe cases in which the intrinsic surface energetics dominate, and the contribution of external loading to the surface-energy variation is correspondingly weaker.

Overall, Fig. 3 shows that the present framework can unify several apparently different adhesion behaviors within a single energy-based description. By incorporating the normal-load-induced variation of solid–liquid interfacial tension into the interfacial energy landscape, the model predicts the adhesion-force ratio directly from the corresponding energy barrier. It not only reproduces the counterintuitive enhancement of adhesion in the pendant state observed for small droplets but also recovers the Amontons-like regime under other parameter settings. In this way, our model provides a physically transparent link between intrinsic surface energetics, load sensitivity, and the resulting adhesion response.

B. K–F model generalization

In Young's law, the presence of gas is neglected at the solid–liquid interface, corresponding to $\phi_L = 1$; at the solid–gas interface, $\phi_G = 1$. Thus, the solid–liquid and solid–gas interfacial tensions are defined with the condition $\phi_L = 1$ and $\phi_G = 0$. Under this idealized condition, a pressure-independent $\triangle\gamma$ is derived as

$$\triangle\gamma = lf_S[(\varepsilon_G + \chi_{SG}) - (\varepsilon_L + \chi_{SL})] = lf_S(\triangle\varepsilon + \triangle\chi).$$

Defining the liquid–gas surface tension as $\sigma \approx l'\chi_{LG}$ (χ_{LG} is the liquid–gas van der Waals parameter and l' is the liquid–gas interface thickness), the famous Young's law is obtained,

$$\cos\theta_Y = \frac{\triangle\gamma}{\sigma} = \frac{lf_S(\triangle\varepsilon + \triangle\chi)}{l'\chi_{LG}}. \tag{15}$$

Within our framework of surface tension, the difference between the solid–liquid and solid–gas interfacial tensions is expressed as

$$\langle\triangle\gamma\rangle = l\chi_{LG}[(\langle\phi_L\rangle - \langle\phi_G\rangle)(\langle\phi_L\rangle + \langle\phi_G\rangle - 2\eta)].$$

At the saddle point, the average solid–liquid and solid–gas interfacial tensions become equal, indicating that the lateral load and adhesion are balanced. This feature of this state corresponds to the critical sliding state, in which any infinitesimal energy input is sufficient to initiate droplet motion. The criterion $\langle\triangle\gamma\rangle = 0$ implies two roots. The first one is $\langle\phi_L\rangle = \langle\phi_G\rangle$, implying the formation of a microscopic lubrication-like interfacial state.

The other one reads $\langle\phi_L\rangle + \langle\phi_G\rangle = 2\eta$. The parameter η can be split into two terms: $\eta = \eta_Y + \eta_\varphi$, where η_Y and η_φ are expressed as

$$2\eta_Y = 1 - \frac{f_S(\triangle\varepsilon + \triangle\chi)}{\chi_{LG}},\quad 2\eta_\varphi = \frac{f_S}{\chi_{LG}}\left(\frac{2\sigma}{R} + \frac{\rho V}{\pi r_c^2}a_\perp + p_\varphi\right).$$

Here, η_φ denotes the corresponding value evaluated along the droplet contact line at the angular position φ in cylindrical coordinates. Variations in η originate from the pressure non-uniformity, p_φ, within the adsorption layer. For a three-dimensional droplet, as shown in Fig. 4, the local pressure distribution along the contact line is given by

$$p_\varphi = \rho a_\parallel r_c \cos\varphi. \tag{16}$$

Substituting Eq. (16) into the expression for η_φ, the angular distribution of the interfacial parameter induced by the pressure non-uniformity becomes

$$2\eta_\varphi = \frac{f_S}{\chi_{LG}}\left(\frac{2\sigma}{R} + \frac{\rho V}{\pi r_c^2}a_\perp + \rho a_\parallel r_c\cos\varphi\right). \tag{17}$$

Using the expression for η_Y in Eq. (15), the Young contact angle can be written as

$$\cos\theta_Y = \frac{l}{l'}(1 - 2\eta_Y). \tag{18}$$

Similarly, substituting η_φ into Eq. (15) gives the contact-angle distribution along the three-phase contact line at angular position φ in cylindrical coordinates,

$$\cos\theta_\varphi = \frac{l}{l'}[1 - 2(\eta_Y + \eta_\varphi)]. \tag{19}$$

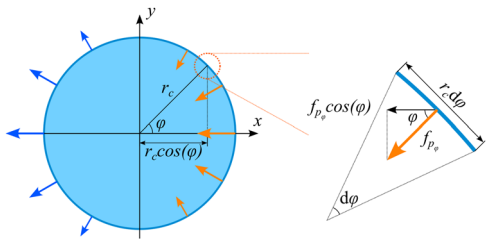

FIG. 4. Schematic of a droplet on a substrate: the left panel shows the projection of the droplet on the substrate surface, with arrows around the perimeter indicating the magnitude of pinning forces along the three-phase contact line. The orange arrows represent the pinning force on the advancing side, and the blue arrows represent the pinning force on the receding edge. φ denotes the angular position in a cylindrical coordinate system. The right panel is a magnified view of a local segment, illustrating the contribution of the pinning force on a line element (orange arrow) to the transverse resistance (black arrow).

In classical theories, the pinning force per unit length of the contact line is written as[61–64]

$$f_P = \sigma(\cos\theta - \cos\theta_Y), \tag{20}$$

where θ is the apparent contact angle, and θ_Y is Young's contact angle. The deviation of the apparent contact angle is considered to represent the intensity of the pinning force with this equation.

Using Eq. (20), together with the contact-angle expressions in Eqs. (18) and (19), the pinning-force distribution along the contact line is obtained as

$$f_{P_\varphi} = -\frac{2\sigma}{R}l^* - \frac{\rho V}{\pi r_c^2}a_\perp l^* - \rho a_\parallel r_c \cos\varphi\, l^*. \tag{21}$$

Here, $l^* = f_S l$ denotes the modified adsorption layer thickness. Integrating the component of the pinning force along the loading direction over the entire three-phase contact line gives

$$F_\parallel = \int_0^{2\pi} f_{P_\varphi}\cos\varphi r_c \mathrm{d}\varphi = -\rho a_\parallel \pi r_c^2 l^*. \tag{22}$$

The integrated force has the same magnitude as the externally applied lateral load, which strongly supports the validity of the present expression for the local pinning force along the contact line. Comparing Eq. (22) with the lateral adhesion required to balance the external load, $F_\parallel = \rho a_\parallel V$, and using the expression for the droplet volume, we obtain

$$l^* = \frac{V}{\pi r_c^2} = \frac{r_c}{3}\frac{(2+\cos\theta)(1-\cos\theta)^2}{\sin^3\theta}. \tag{23}$$

The advancing and receding edges of the droplet correspond to the locations $\varphi = 0$ and $\varphi = \pi$, respectively. Substituting these values of φ into Eq. (19) gives the expressions for the advancing and receding contact angles,

$$\cos\theta_+ = \frac{l}{l'}[1 - 2(\eta_Y + \eta_{\varphi=0})], \tag{24}$$

$$\cos\theta_- = \frac{l}{l'}[1 - 2(\eta_Y + \eta_{\varphi=\pi})]. \tag{25}$$

Similarly, substituting $\varphi = 0$ and $\varphi = \pi$ into the pinning-force expression, Eq. (21), yields the pinning forces at the advancing and receding edges,

$$f_{P_\pm} = -\frac{2\sigma}{R}l^* - \frac{\rho V}{\pi r_c^2}a_\perp l^* \mp \rho a_\parallel r_c l^*. \tag{26}$$

Here, f_{P_+} and f_{P_-} denote the pinning forces at the advancing (+) and receding (−) edges, respectively. By averaging Eq. (26), we obtain the mean pinning force $|f_p|$, thereby enabling direct comparison with the experimental results. In Fig. 5(a), the experimental pinning force data[32] for small droplets with volume ranging from 0.5 to 3 μl are compared with the prediction of Eq. (26). The values of α and $\alpha/(2\eta_{+g})$ are adjusted according to the corresponding droplet volume. The model is in good agreement with the experimental measurements.

Comparing our result, Eq. (26), with the classical definition, Eq. (20), we recover the Kawasaki–Furmidge (K–F) equation,[65–69]

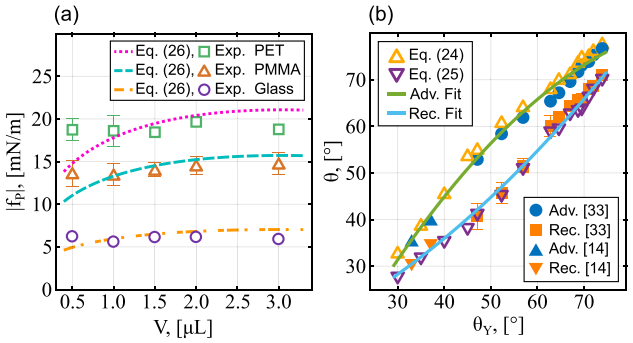

FIG. 5. (a) Pinning force at the droplet contact line as a function of droplet volume. Markers represent experimental results;[32] unless otherwise noted, the corresponding error bars are smaller than the marker size. The lines show the pinning force calculated from Eq. (26). (b) Advancing (θ_+) and receding (θ_-) contact angles as functions of the Young contact angle θ_Y. Solid markers denote experimental measurements obtained on relatively smooth surfaces;[14,33] unless otherwise noted, the corresponding error bars are smaller than the marker size. Open markers represent theoretical reconstructions, and the lines indicate second-order polynomial fits to the theoretical data.

$$F_\parallel = \rho a_\parallel V = kW\sigma(\cos\theta_- - \cos\theta_+), \tag{27}$$

where $W = 2r_c$ denotes the droplet width and

$$k = \frac{V}{4r_c^2 l^*}$$

is a geometry-dependent parameter. This definition gives k a clear mechanistic meaning, linking the macroscopic droplet size to the microscopic adsorption-layer thickness. Moreover, by substituting the expression for l^* from Eq. (23), we obtain

$$k = \frac{\pi}{4}, \tag{28}$$

which is in agreement with the values of k reported in many previous studies for small droplets,[16,32,70,71] thereby providing further support for the present framework. Therefore, the second solution of $\langle\triangle\gamma\rangle = 0$ reveals the origin of the pinning force along the droplet three-phase contact line and recovers the traditional Kawasaki–Furmidge relation used to describe droplet adhesion on a substrate.

Our theory suggests that droplet sliding is initiated only when both conditions, $\langle\phi_L\rangle = \langle\phi_G\rangle$ and the Kawasaki–Furmidge (K–F) relation, are satisfied. In this sense, the classical K–F equation provides only a partial criterion, as it treats sliding as a balance of body forces even in the small-droplet regime, where bulk energy is negligible. By contrast, the present theory derives the sliding criterion from the pressure non-uniformity induced by lateral loading and its effect on the interfacial-energy distribution at the droplet base. This framework not only gives a clearer physical interpretation of the empirical parameter k but also yields a self-consistent sliding criterion grounded in interfacial energetics.

As previously mentioned, the lateral-load-induced non-uniform pressure changes the local compositions ϕ_L and ϕ_G within the adsorption layer. Within this adsorption layer (not in the bulk), the non-uniform pressure is compensated by the Young–Laplace

TABLE I. Representative mechanisms of contact-angle hysteresis.

Mechanism	Applicable system
Roughness	Rough solid surfaces; contact-line pinning by surface topography
Chemical heterogeneity	Chemically patterned or defective surfaces; pinning by spatial variation of surface energy
Cassie–Wenzelstate	Textured hydrophobic or superhydrophobic surfaces; hysteresis depends on air trapping or liquid penetration
Presentadsorption-layermechanism	Ideal rigid, smooth, and chemically homogeneous surfaces; intrinsic interfacial contribution from the adsorption layer

pressure through surface curvature adjustments, leading to contact angle hysteresis [Fig. 6(a), Appendix A].

Figure 5(b) shows how the advancing contact angle, θ_+, and receding contact angle, θ_-, vary with Young's contact angle, θ_Y. The reconstructed values of θ_+ and θ_- are calculated with Eqs. (24) and (25). Unless otherwise stated, $a_\perp$ is taken as $+g$, and the corresponding $a_\parallel$ is determined from the K–F relation based on experimentally measured contact angle hysteresis data.[14,33] The hysteresis, $\theta_+ - \theta_-$, decreases as θ_Y approaches 0° or 90°, consistent with experimental observations. Mechanistically, the contact angle hysteresis greater than 10° observed in experiments on relatively smooth substrates is unlikely to be caused by the Young–Laplace pressure in the bulk liquid. For small droplets ($Bo \ll 1$), the surface area A of the droplet cap remains nearly constant, and the Young–Laplace pressure in the bulk liquid remains nearly unchanged. However, variations in the compositions ϕ_L and ϕ_G within the adsorption layer can generate significant pressure differences, leading to pronounced contact angle hysteresis.

It is important to distinguish the present mechanism from the well-established extrinsic origins of contact-angle hysteresis. On real surfaces, contact-angle hysteresis is often dominated by roughness,[7,72] chemical heterogeneity,[8] Wenzel–Cassie state transitions,[13,73] and surface adaptation,[21] as shown in Table I. These mechanisms may generate hysteresis over very different angular ranges. For example, optimized Cassie-type superhydrophobic surfaces may exhibit nearly vanishing hysteresis, whereas Wenzel states, dense microtextures, or designed defects can produce hysteresis of tens of degrees. Therefore, the magnitude of CAH is not universal but depends on the dominant microscopic pinning or adaptation mechanism.

The mechanism proposed in this work should be understood as an intrinsic interfacial contribution associated with the adsorption layer on an ideally smooth and chemically homogeneous surface. It is not intended to replace roughness- or heterogeneity-induced hysteresis on real substrates. Rather, it describes the limiting case in which no explicit macroscopic defect or roughness is introduced. The predicted angular shift is only of the order of a few degrees, which is much smaller than the hysteresis caused by strong defects or Cassie–Wenzel pinning but remains experimentally resolvable with high-precision contact-angle measurements.[14,33] Thus, in practical systems, the total observed CAH should be regarded as the combined result of the present adsorption-layer contribution and additional extrinsic contributions from roughness, chemical heterogeneity, or Cassie–Wenzel wetting states.

IV. CONCLUSION

In summary, we have developed a microscopic mean-field theory of adhesion at solid–liquid interfaces and proposed a sliding criterion for droplet motion on solid surfaces (within the small-droplet limit),

$$\langle \triangle \gamma \rangle = 0.$$

Physically, this criterion indicates that sliding is initiated when external loading drives the adsorption layer beneath the droplet into a microscopic lubrication-like interfacial state. The proposed framework captures the dependence of adhesion on the applied normal load, explains previously counterintuitive experimental observations, and recovers an Amontons-like regime in the appropriate limit. It reproduces the classical K–F relation, predicts both the pinning force and contact-angle hysteresis, and provides a clearer physical interpretation of the empirical parameter k in the K–F equation. Moreover, the present theory resolves the fundamental inconsistency of applying body–force balance to small droplets, for which body-energy contributions are negligible, and shows excellent agreement with experiments under diverse conditions. Taken together, these results establish both the physical consistency and the practical applicability of the proposed theoretical framework.

ACKNOWLEDGMENTS

R.Y. acknowledges the funding through the Gottfried-Wilhelm Leibniz Prize (No. NE 822/31-1) of the German Research Foundation (DFG). F.W. acknowledges the funding from the Virt-Mat project "VirtMat P09: Wetting Phenomena" of the Helmholtz Association under the program "MSE—Materials Science and Engineering" (No. 43.31.01). R.Y. is grateful to Mr. Lisen Bi and Dr. Haodong Zhang for their valuable discussions.

AUTHOR DECLARATIONS

Conflict of Interest

The authors have no conflicts to disclose.

Author Contributions

R.Y. derived the equations, analyzed the data, and prepared the original paper. F.W. proposed the energy map method and the core concept of $\langle \triangle\gamma \rangle = 0$, demonstrated its equivalence to the Kawasaki–Furmidge equation, revised the paper, and supervised the project. B.N. contributed to paper improvement, secured funding, and supervised the project.

Ruize Yin: Conceptualization (supporting); Formal analysis (lead); Methodology (equal); Visualization (lead); Writing – original draft (lead); Writing – review & editing (supporting). **Fei Wang**: Conceptualization (lead); Formal analysis (supporting); Methodology (equal); Supervision (lead); Writing – review & editing (lead). **Britta Nestler**: Funding acquisition (lead); Supervision (supporting); Writing – review & editing (supporting).

DATA AVAILABILITY

No new experimental data were generated in this study. The experimental data used for comparison were taken from the cited literature. The data and MATLAB scripts that support the findings of this article are openly available in Github at https://github.com/Yin-Ruize/A-Microscopic-Mean-Field-Theory-of-Small-Droplet-Adhesion-on-Solid-Surfaces, Ref. 77.

NOMENCLATURE

A	Liquid–gas interfacial area (m^2)
α	Intrinsic dimensionless interfacial parameter (dimensionless)
$a_\perp, a_\parallel$	Normal and lateral accelerations ($m\ s^{-2}$)
$F_\perp, F_\parallel$	Total normal and lateral forces (N)
f_S	Correction factor due to the solid-phase volume fraction (dimensionless)
f_{P_φ}	Local pinning force per unit contact-line length ($N\ m^{-1}$)
l, l^*, l'	Adsorption-layer, modified adsorption-layer, and liquid–gas interfacial thickness (m)
R	Liquid–gas curvature radius (m)
r_c	Contact radius (m)
S_1, S_2, S_3	Wetted, droplet-affected, and far-field substrate areas (m^2)
V	Droplet volume (m^3)
σ	Liquid–gas interfacial tension/free-energy density ($N\ m^{-1} = J\ m^{-2}$)
γ_{SL}, γ_{SG}	Solid–liquid and solid–gas interfacial free-energy densities ($J\ m^{-2}$)
$\Delta\gamma = \gamma_{SG} - \gamma_{SL}$	Interfacial free-energy difference ($J\ m^{-2}$)
$\langle \Delta\gamma \rangle$	Spatially averaged interfacial free-energy difference over S_1 ($J\ m^{-2}$)
ϕ	Liquid volume fraction in the adsorption layer (dimensionless)
ϕ_L, ϕ_G	Liquid fractions in droplet-covered and gas-covered adsorption-layer regions (dimensionless)
φ	Angular coordinate along the contact line (rad)
$\varepsilon, p, \chi_{ij}$	Internal, pressure, and interaction energy densities in the adsorption layer ($J\ m^{-3}$)
$\eta, \eta_Y, \eta_\varphi$	Effective dimensionless interfacial parameters (dimensionless)
θ_{tilt}	Critical roll-off angle in the K–F relation (rad or degree)

APPENDIX A: ELLIPTIC SHAPE ASSUMPTION

A lateral load alters the local composition at the advancing η_+ and receding η_- sides, resulting in pressure non-uniformity in the adsorption layer. To restore equilibrium, the interface curvature adjusts such that the Young–Laplace pressure compensates for the gradient. Consequently, the local contact angles deviate from Young's contact angle, giving rise to distinct advancing θ_+ and receding θ_- angles within the adsorption layer. These angles are then transmitted across the Gibbs dividing surface for macroscopic contact angle measurement through imaging or visual observation [Fig. 6(a)].

For the liquid–gas interface, the classical gravity-deformed ellipsoidal shape[20,58,74–76] is extended to a tilted ellipsoid under a normal and lateral combined load [Fig. 6(b)]. The parameters a, b, and c denote the semiaxis lengths of the ellipsoid along the x, y, and z directions, respectively; h is the distance from the ellipsoid center to the upper surface of the substrate; and ψ represents the tilt angle of the ellipsoid relative to the vertical axis, as shown in Fig. 6(b). The tilted ellipsoid function is

$$\frac{(x\cos\psi + z'\sin\psi)^2}{a^2} + \frac{y^2}{b^2} + \frac{(x\sin\psi - z'\cos\psi)^2}{c^2} = 1,$$

with $z' = z + h$.

For small droplets, footprint deformation is negligible; thus, the base shape is treated as unchanged, and volume conservation constrains the profile, yielding an approximately elliptical cap. For example, for a 0.5 μl hexadecane droplet with a Young's contact angle of 33°, an advancing angle of 35.5°, and a receding angle of 30.3° (as in Tadmor's experiments[14]), the difference in liquid–gas interfacial area between the elliptical and spherical-cap shapes is less than 2% and corresponds to an interfacial-energy change below

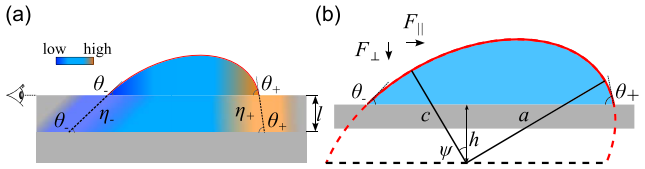

FIG. 6. (a) Schematic of a droplet under lateral load. The adsorption layer composition changes at the advancing edge, η_+, and at the receding edge, η_-, resulting in pressure non-uniformity within the adsorption layer; θ_+ and θ_- are the resulting contact angles at the advancing and receding edges, respectively. Dark blue represents low pressure regions, and orange denotes high pressure regions. This provides a bottom-up understanding of contact angle hysteresis, linking its origin in the adsorption layer to the resulting macroscopic contact angle. (b) Cross section of a 3D ellipsoidal droplet under normal load $F_\perp$ and lateral load $F_\parallel$.

1 nJ. This surface-energy variation is negligible compared with the load-induced surface-energy change at the base.

Under Tadmor's experimental conditions, we consider a hexadecane droplet with

$$V = 0.5\ \mu\text{l},$$
$$\rho = 800\ \text{kg m}^{-3},$$
$$g = 9.81\ \text{m s}^{-2}.$$

For spherical-cap droplets of volume V with Young's contact angles of 33° and 37°, the corresponding change in the center-of-mass height gives a gravitational potential-energy difference of

$$\Delta E_g = E_g(37^\circ) - E_g(33^\circ) \approx 2.6 \times 10^{-11}\ \text{J} = 2.6 \times 10^{-2}\ \text{nJ}.$$

In comparison, the change of surface energy, E_{base}, is at least in the scale of tens of nanojoules, as shown in Fig. 2. Therefore, $\Delta E_g/E_{base}$ is less than 1%, showing that the gravitational contribution associated with the change in the center-of-mass height is negligible compared with the surface energy variation. For the normal load, the relevant pressure scale is

$$p_g \approx \frac{\rho V g}{\pi r_c^2} \approx 1\ \text{Pa}.$$

This value is of the same order of magnitude as the lateral-load-induced pressure perturbation considered in the present model. Both load-induced pressure scales are much smaller than the nearly uniform Laplace-pressure, or capillary-pressure, scale,

$$\frac{2\sigma}{R} \approx 30\ \text{Pa},$$

in the small-Bond-number regime. Therefore, these pressure perturbations do not significantly deform the liquid–gas interface. Nevertheless, they are retained in the adsorption-layer free-energy density because they represent load-dependent pressure contributions that are conjugate to the adsorption-layer volume.

APPENDIX B: PRESSURE CONTRIBUTION TO SURFACE FREE-ENERGY

Because pressure is thermodynamically conjugate to volume, it cannot be neglected in the free-energy description of an equilibrium droplet. Treating the adsorption layer as a distinct phase, its volume constraint is incorporated explicitly in the variational formulation through a Lagrange multiplier. Accordingly, we introduce the constrained free-energy functional,

$$\mathscr{G} = \mathscr{F} + \lambda V = \int (\varepsilon + \chi)\ \mathrm{d}\phi + l \int p\ \mathrm{d}S,$$

where $\mathscr{F} = \int(\varepsilon + \chi)\,\mathrm{d}\phi$ denotes the intrinsic free-energy functional of the adsorption layer, including the internal-energy contribution ε and the van der Waals interaction energy χ; $V = l\int \mathrm{d}S$ is the volume of the adsorption-layer phase, with l being its thickness; and λ is the Lagrange multiplier associated with the volume constraint. At mechanical equilibrium, λ is identified with the effective pressure-related contribution p, conjugate to the adsorption-layer volume, including the Young–Laplace pressure difference and any externally imposed loading. Therefore, the pressure contribution is not an extraneous correction but an intrinsic part of the equilibrium free-energy description.

APPENDIX C: SOLID PHASE VOLUME FRACTION

The total energy density of the adsorption layer is given by the sum of the internal, van der Waals, and pressure energies. By defining the solid phase fraction in the adsorption layer as ϕ_S, the liquid phase fraction is $\phi(1-\phi_S)$, and the gas phase fraction is $(1-\phi)\ (1-\phi_S)$, where ϕ represents the volume fraction of liquid phase in the liquid–gas mixture in the adsorption layer. Using the interfacial energy density in the form of Eq. (9), the internal, van der Waals, and pressure contributions can be written as

$$\varepsilon(\phi) = \varepsilon_L\phi(1-\phi_S) + \varepsilon_G(1-\phi)(1-\phi_S) + \varepsilon_S\phi_S,$$
$$\chi(\phi) = (1-\phi_S)[\chi_{LG}\phi(1-\phi)(1-\phi_S) + \chi_{SL}\phi + \chi_{SG}(1-\phi)],$$
$$p(\phi) = p_L\phi(1-\phi_S) + p_G(1-\phi)(1-\phi_S) + p_S\phi_S.$$

In the droplet-sliding scenario, deformation and compression of the solid phase are neglected. Accordingly, the terms $\varepsilon_S\phi_S$ and $P_S\phi_S$ are treated as constant references and omitted in the following discussion. Moreover, the liquid–gas van der Waals term, $\chi_{LG}\phi(1-\phi)(1-\phi_S)^2$, is the only contribution containing the factor $(1-\phi_S)^2$. By defining $f_S = 1/(1-\phi_S)$ and multiplying the entire expression by f_S^2, the resulting form reduces to Eq. (10).

APPENDIX D: DERIVATION FOR THE FORCE RATIO $\Lambda \approx F_{\|a_\perp}/F_{\|+g}$

As described in the main text, the exact expression of the energy minimum state can be obtained for two local minimal points,

$$E_1 : \langle\phi_L\rangle = 0, \langle\phi_G\rangle = \eta,\ E_2 : \langle\phi_L\rangle = 1,\ \langle\phi_G\rangle = \eta.$$

The saddle point, $E_S : \langle\phi_L\rangle = \eta, \langle\phi_G\rangle = \eta$, separates the two local minima.

A sessile state yields $E_{\min} = E_1$ at $\langle\phi_L\rangle = 0$ and, therefore, $\triangle E_1 = E_S - E_1 = l\chi_{LG}\eta^2 S_1$. For the pendant state, it follows $E_{\min} = E_2$ at $\langle\phi_L\rangle = 1$ and, therefore, $\triangle E_2 = E_S - E_2 = l\chi_{LG}(1-\eta)^2 S_1$.

More specifically, the critical force can be estimated as

$$F_{\|a_\perp} \approx \frac{\Delta E_{a_\perp}}{\ell_c(a_\perp)},$$

where $\Delta E_{a_\perp}$ is the energy barrier defined from the energy landscape and $\ell_c(a_\perp)$ is the characteristic lateral displacement, or reaction-path length, over which the external lateral work is performed before sliding. Therefore, the more general form of Eq. (14) should read

$$\frac{F_{\|a_\perp}}{F_{\|+g}} = \frac{\Delta E_{a_\perp}}{\Delta E_{+g}} \frac{\ell_c(+g)}{\ell_c(a_\perp)}.$$

For the small droplets considered in this work, the deformation at the critical sliding state is very weak under different normal loads. Therefore, $\ell_c(a_\perp)$ changes only negligibly with $a_\perp$, and the above expression reduces to Eq. (14).

The droplet adhesion force $F_{\|a_\perp}$ is calculated for the normal load $a_\perp$. This adhesion force is scaled by that when $a_\perp = +g$. Thus, the following force ratio is obtained:

$$\Lambda = \frac{F_{\|a_\perp}}{F_{\|+g}} \approx \begin{cases} \left(\frac{\alpha + \xi a_\perp}{\alpha + \xi g}\right)^2, & E_1 < E_2, \\ \left(\frac{1 - \alpha - \xi a_\perp}{\alpha + \xi g}\right)^2, & E_1 > E_2, \end{cases}$$

where $\xi = f_S \rho V / (\pi r_c^2 \chi_{LG})$.

REFERENCES

[1] H.-J. Butt, R. Berger, J. De Coninck, and R. Tadmor, "Drop friction," Nat. Rev. Phys. **7**, 425–438 (2025).
[2] R. de la Madrid, F. Garza, J. Kirk, H. Luong, L. Snowden, J. Taylor, and B. Vizena, "Comparison of the lateral retention forces on sessile, pendant, and inverted sessile drops," Langmuir **35**(7), 2871–2877 (2019).
[3] N. Gao, F. Geyer, D. W. Pilat, S. Wooh, D. Vollmer, H.-J. Butt, and R. Berger, "How drops start sliding over solid surfaces," Nat. Phys. **14**(2), 191–196 (2018).
[4] F. Wang, Y. Wu, and B. Nestler, "Wetting effect on patterned substrates," Adv. Mater. **35**(25), 2210745 (2023).
[5] Q. Lu, B. Sanogo, T. Kumar, B. B. Xu, and X. Zhang, "Recent advances in reactive microdroplets for clean water and energy," Adv. Mater. **37**, e09486 (2025).
[6] R. Tadmor, "Open problems in wetting phenomena: Pinning retention forces," Langmuir **37**(21), 6357–6372 (2021).
[7] J. F. Joanny and P. G. de Gennes, "A model for contact angle hysteresis," J. Chem. Phys. **81**(1), 552–562 (1984).
[8] H.-J. Butt, J. Liu, K. Koynov, B. Straub, C. Hinduja, I. Roismann, R. Berger, X. Li, D. Vollmer, W. Steffen, and M. Kappl, "Contact angle hysteresis," Curr. Opin. Colloid Interface Sci. **59**, 101574 (2022).
[9] P. G. De Gennes, "Wetting: Statics and dynamics," Rev. Mod. Phys. **57**(3), 827–863 (1985).
[10] K. Kawasaki, "Study of wettability of polymers by sliding of water drop," J. Colloid Sci. **15**(5), 402–407 (1960).
[11] C. G. L. Furmidge, "Studies at phase interfaces. I. The sliding of liquid drops on solid surfaces and a theory for spray retention," J. Colloid Sci. **17**(4), 309–324 (1962).
[12] T. Mouterde, P. S. Raux, C. Clanet, and D. Quéré, "Superhydrophobic frictions," Proc. Natl. Acad. Sci. U. S. A. **116**(17), 8220–8223 (2019).
[13] L. Bi, F. Wang, and B. Nestler, "Wetting transition: Macroscopic roughness, static friction, and energy barrier," Phys. Rev. Res. **7**(4), 043093 (2025).
[14] R. Tadmor, P. Bahadur, A. Leh, H. E. N'guessan, R. Jaini, and L. Dang, "Measurement of lateral adhesion forces at the interface between a liquid drop and a substrate," Phys. Rev. Lett. **103**(26), 266101 (2009).
[15] G. McHale, N. Gao, G. G. Wells, H. Barrio-Zhang, and R. Ledesma-Aguilar, "Friction coefficients for droplets on solids: The liquid–solid amontons' laws," Langmuir **38**(14), 4425–4433 (2022).
[16] Y. Stern, R. Tadmor, A. Miron, and A. Vinod, "Furmidge equation revisited," Langmuir **41**(18), 11785–11793 (2025).
[17] A. I. ElSherbini and A. M. Jacobi, "Retention forces and contact angles for critical liquid drops on non-horizontal surfaces," J. Colloid Interface Sci. **299**(2), 841–849 (2006).
[18] D. 't Mannetje, A. Banpurkar, H. Koppelman, M. H. G. Duits, D. van den Ende, and F. Mugele, "Electrically tunable wetting defects characterized by a simple capillary force sensor," Langmuir **29**(31), 9944–9949 (2013).
[19] C. W. Extrand and Y. Kumagai, "Liquid drops on an inclined plane: The relation between contact angles, drop shape, and retentive force," J. Colloid Interface Sci. **170**(2), 515–521 (1995).
[20] E. M. Blokhuis, Y. Shilkrot, and B. Widom, "Young's law with gravity," Mol. Phys. **86**, 891–899 (1995).
[21] H.-J. Butt, R. Berger, W. Steffen, D. Vollmer, and S. A. L. Weber, "Adaptive wetting—Adaptation in wetting," Langmuir **34**(38), 11292–11304 (2018).
[22] D. Lohse and X. Zhang, "Physicochemical hydrodynamics of droplets out of equilibrium," Nat. Rev. Phys. **2**(8), 426–443 (2020).
[23] Y. Wu, H. Zhang, F. Wang, and B. Nestler, "Unveiling the complex morphologies of sessile droplets on heterogeneous surfaces," Commun. Phys. **8**(1), 38 (2025).
[24] W. S. Y. Wong, L. Hauer, A. Naga, A. Kaltbeitzel, P. Baumli, R. Berger, M. D'Acunzi, D. Vollmer, and H.-J. Butt, "Adaptive wetting of polydimethylsiloxane," Langmuir **36**(26), 7236–7245 (2020).
[25] D. Seveno, T. D. Blake, and J. De Coninck, "Young's equation at the nanoscale," Phys. Rev. Lett. **111**(9), 096101 (2013).
[26] D. Bonn, "Wetting transitions," Curr. Opin. Colloid Interface Sci. **6**(1), 22–27 (2001).
[27] T.-S. Wong, S. H. Kang, S. K. Y. Tang, E. J. Smythe, B. D. Hatton, A. Grinthal, and J. Aizenberg, "Bioinspired self-repairing slippery surfaces with pressure-stable omniphobicity," Nature **477**(7365), 443–447 (2011).
[28] F. Wang and B. Nestler, "Wetting and contact-angle hysteresis: Density asymmetry and van der Waals force," Phys. Rev. Lett. **132**(12), 126202 (2024).
[29] F. Wang, H. Zhang, and B. Nestler, "Wetting phenomena: Line tension and gravitational effect," Phys. Rev. Lett. **133**(24), 246201 (2024).
[30] H. Tan, D. Lohse, and X. Zhang, "Self-lubricating drops," Curr. Opin. Colloid Interface Sci. **68**, 101744 (2023).
[31] P. Lv, P. Peñas, H. Le The, J. Eijkel, A. van den Berg, X. Zhang, and D. Lohse, "Self-propelled detachment upon coalescence of surface bubbles," Phys. Rev. Lett. **127**(23), 235501 (2021).
[32] C. W. Extrand and A. N. Gent, "Retention of liquid drops by solid surfaces," J. Colloid Interface Sci. **138**(2), 431–442 (1990).
[33] C. N. C. Lam, R. Wu, D. Li, M. L. Hair, and A. W. Neumann, "Study of the advancing and receding contact angles: Liquid sorption as a cause of contact angle hysteresis," Adv. Colloid Interface Sci. **96**(1-3), 169–191 (2002).
[34] F. Aurbach, F. Wang, and B. Nestler, "Wetting phenomena of droplets and gas bubbles: Contact angle hysteresis based on varying liquid–solid and solid–gas interfacial tensions," J. Chem. Phys. **161**(16), 164708 (2024).
[35] A. W. Adamson and A. P. Gast, *Physical Chemistry of Surfaces*, 6th ed. (Wiley, New York, 1997).
[36] P.-G. de Gennes, F. Brochard-Wyart, and D. Quéré, *Capillarity and Wetting Phenomena: Drops, Bubbles, Pearls, Waves* (Springer, New York, 2003).
[37] J. Willard Gibbs, *The Collected Works of J. Willard Gibbs, Volume 1: Thermodynamics* (Longmans, Green and Co, New York, 1928).
[38] J. D. van der Waals and J. S. Rowlinson, *On the Continuity of the Gaseous and Liquid States* (Courier Corporation, 2004) .
[39] J. D. Van Der Waals, "The thermodynamic theory of capillarity under the hypothesis of a continuous variation of density," J. Stat. Phys. **20**(2), 200–244 (1979).
[40] J. W. Cahn and J. E. Hilliard, "Free energy of a nonuniform system. I. Interfacial free energy," J. Chem. Phys. **28**(2), 258–267 (1958).
[41] P. Yue, "Thermodynamically consistent phase-field modelling of contact angle hysteresis," J. Fluid Mech. **899**, A15 (2020).
[42] F. Wang, H. Zhang, Y. Wu, and B. Nestler, "A thermodynamically consistent diffuse interface model for the wetting phenomenon of miscible and immiscible ternary fluids," J. Fluid Mech. **970**, A17 (2023).
[43] H. Zhang, F. Wang, and B. Nestler, "Line tension of sessile droplets: Thermodynamic considerations," Phys. Rev. E **108**(5), 054121 (2023).
[44] H. Zhang, H. Zhang, F. Wang, and B. Nestler, "Wetting effect induced depletion and adsorption layers: Diffuse interface perspective," Chem. Phys. Chem. **25**(14), e202400086 (2024).
[45] J. W. Cahn, "Critical point wetting," J. Chem. Phys. **66**(8), 3667–3672 (1977).
[46] S. W. Sides, G. S. Grest, and M.-D. Lacasse, "Capillary waves at liquid-vapor interfaces: A molecular dynamics simulation," Phys. Rev. E **60**(6), 6708–6713 (1999).
[47] G. Scocchi, D. Sergi, C. D'Angelo, and A. Ortona, "Wetting and contact-line effects for spherical and cylindrical droplets on graphene layers: A comparative molecular-dynamics investigation," Phys. Rev. E **84**(6), 061602 (2011).
[48] S. Becker, H. M. Urbassek, M. Horsch, and H. Hasse, "Contact angle of sessile drops in Lennard-Jones systems," Langmuir **30**(45), 13606–13614 (2014).
[49] C. Huang, L. Tian, J. Wang, L. Jiang, and K. Zhang, "Water-CO_2 wettability on sandstone surface with asphaltene adsorption: Molecular dynamics simulation," Fuel **360**, 130558 (2024).

[50]J. H. Sikkenk, J. O. Indekeu, J. M. J. van Leeuwen, and E. O. Vossnack, "Molecular-dynamics simulation of wetting and drying at solid-fluid interfaces," Phys. Rev. Lett. **59**(1), 98–101 (1987).
[51]M. Shintaku, H. Oga, H. Kusudo, E. R. Smith, T. Omori, and Y. Yamaguchi, "Measuring line tension: Thermodynamic integration during detachment of a molecular dynamics droplet," J. Chem. Phys. **160**(22), 224502 (2024).
[52]J. Włoch, A. P. Terzyk, M. Wiśniewski, and P. Kowalczyk, "Nanoscale insight into the mechanism of a highly oriented pyrolytic graphite edge surface wetting by 'interferencing' water," Langmuir **33**(34), 8562–8573 (2017).
[53]D. Ross, D. Bonn, and J. Meunier, "Wetting of methanol on the n-alkanes: Observation of short-range critical wetting," J. Chem. Phys. **114**(6), 2784–2792 (2001).
[54]M. R. Moldover and J. W. Cahn, "An interface phase transition: Complete to partial wetting," Science **207**(4435), 1073–1075 (1980).
[55]F. Mugele and J. Heikenfeld, *Electrowetting: Fundamental Principles and Practical Applications* (Wiley, 2018).
[56]P. K. Roy, I. Legchenkova, S. Shoval, L. A. Dombrovsky, and E. Bormashenko, "Osmotic evolution of composite liquid marbles," J. Colloid Interface Sci. **592**, 167–173 (2021).
[57]E. Chibowski and L. Holysz, "Use of the Washburn equation for surface free energy determination," Langmuir **8**(2), 710–716 (1992).
[58]F. Aurbach, F. Wang, and B. Nestler, "Gravitational effect on the equilibrium contact angles of sessile droplets: Theory and simulations," J. Chem. Phys. **163**(3), 034706 (2025).
[59]W. Dong, "Thermodynamics of interfaces extended to nanoscales by introducing integral and differential surface tensions," Proc. Natl. Acad. Sci. U. S. A. **118**(3), e2019873118 (2021).
[60]J. R. Henderson, "Statistical mechanics of the disjoining pressure of a planar film," Phys. Rev. E **72**(5), 051602 (2005).
[61]P. S. Yadav, P. Bahadur, R. Tadmor, K. Chaurasia, and A. Leh, "Drop retention force as a function of drop size," Langmuir **24**(7), 3181–3184 (2008).
[62]B. Zhao, S. Luo, E. Bonaccurso, G. K. Auernhammer, X. Deng, Z. Li, and L. Chen, "Resolving the apparent line tension of sessile droplets and understanding its sign change at a critical wetting angle," Phys. Rev. Lett. **123**(9), 094501 (2019).
[63]E. Bormashenko, "Variational framework for defining contact angles: A general thermodynamic approach," J. Adhes. Sci. Technol. **34**(2), 219–230 (2020).
[64]L. Bi, B. Liu, Z. Zhu, P. E. Theodorakis, H. Hu, and Z. Li, "Molecular dynamics simulation of wenzel-state nanodroplets: Evaporation on heated substrates with different rough structures," Phys. Fluids **35**(1), 012015 (2023).
[65]D. Cortés, M. Kappl, H.-J. Butt, P. Sudersan, and T. P. Corrales, "Friction measurements with picoliter droplets using scanning probe microscopy," Phys. Rev. Lett. **135**(4), 048203 (2025).
[66]S. Tang, Y. Bhimavarapu, S. Gulec, R. Das, J. Liu, H. N'guessan, T. Whitehead, C.-W. Yao, and R. Tadmor, "Droplets sliding down a vertical surface under increasing horizontal forces," Langmuir **35**(25), 8191–8198 (2019).
[67]D. Quéré, "The mobility of drops, pearls, and marbles," Annu. Rev. Condens. Matter Phys. **15**, 291–304 (2024).
[68]M. Backholm, T. Kärki, H. A. Nurmi, M. Vuckovac, V. Turkki, S. Lepikko, V. Jokinen, D. Quéré, J. V. I. Timonen, and R. H. A. Ras, "Toward vanishing droplet friction on repellent surfaces," Proc. Natl. Acad. Sci. U. S. A. **121**(17), e2315214121 (2024).
[69]A. Keiser, P. Baumli, D. Vollmer, and D. Quéré, "Universality of friction laws on liquid-infused materials," Phys. Rev. Fluids **5**(1), 014005 (2020).
[70]X. Li, F. Bodziony, M. Yin, H. Marschall, R. Berger, and H.-J. Butt, "Kinetic drop friction," Nat. Commun. **14**(1), 4571 (2023).
[71]G. McHale, G. G. Wells, and R. Ledesma-Aguilar, "Surfaces slippery to liquids: Wettability, adhesion, and contact line friction," Langmuir **41**(23), 14579–14588 (2025).
[72]D. J. E. Harvie, "Contact-angle hysteresis on rough surfaces: Mechanical energy balance framework," J. Fluid Mech. **986**, A17 (2024).
[73]L. Bi, F. Wang, and B. Nestler, "Surface morphology control of the Cassie–Wenzel transition: An energy landscape perspective," J. Chem. Phys. **164**(9), 094701 (2026).
[74]Y. Yang, C. Lv, L. Wang, and P. Li, "The shape of heavy droplets on superhydrophobic surfaces," ACS Omega **5**(41), 26732–26737 (2020).
[75]G. Whyman and E. Bormashenko, "Oblate spheroid model for calculation of the shape and contact angles of heavy droplets," J. Colloid Interface Sci. **331**(1), 174–177 (2009).
[76]V. A. Lubarda and K. A. Talke, "Analysis of the equilibrium droplet shape based on an ellipsoidal droplet model," Langmuir **27**(17), 10705–10713 (2011).
[77]"Droplet friction," MATLAB code, GitHub, https://github.com/Yin-Ruize/A-Microscopic-Mean-Field-Theory-of-Small-Droplet-Adhesion-on-Solid-Surfaces (2026).